THE JOURNAL OF BIOLOGICAL CHEMISTRY VOL. 288, NO. 13, pp. 9383–9395, March 29, 2013

F_1-ATPase of *Escherichia coli*

*THE ϵ-INHIBITED STATE FORMS AFTER ATP HYDROLYSIS, IS DISTINCT FROM THE ADP-INHIBITED STATE, AND RESPONDS DYNAMICALLY TO CATALYTIC SITE LIGANDS**[S]

Received for publication, January 16, 2013, and in revised form, February 5, 2013 Published, JBC Papers in Press, February 11, 2013, DOI 10.1074/jbc.M113.451583

Naman B. Shah, Marcus L. Hutcheon, Brian K. Haarer, and Thomas M. Duncan[1]

From the Department of Biochemistry and Molecular Biology, State University of New York Upstate Medical University, Syracuse, New York 13210

Background: Bacterial ATP synthases are autoinhibited by the subunit ϵ C-terminal domain.
Results: Nucleotide hydrolysis is required to form the ϵ-inhibited state, which also responds dynamically to different ligand conditions.
Conclusion: ϵ inhibition initiates at the catalytic dwell angle, but reversible rotation over ~40° is probably involved in nucleotide effects on the inhibitory state of ϵ.
Significance: ϵ inhibition may provide a new target for antimicrobial discovery.

F_1-ATPase is the catalytic complex of rotary nanomotor ATP synthases. Bacterial ATP synthases can be autoinhibited by the C-terminal domain of subunit ϵ, which partially inserts into the enzyme's central rotor cavity to block functional subunit rotation. Using a kinetic, optical assay of F_1·ϵ binding and dissociation, we show that formation of the extended, inhibitory conformation of ϵ ($ϵ_X$) initiates after ATP hydrolysis at the catalytic dwell step. Prehydrolysis conditions prevent formation of the $ϵ_X$ state, and post-hydrolysis conditions stabilize it. We also show that ϵ inhibition and ADP inhibition are distinct, competing processes that can follow the catalytic dwell. We show that the N-terminal domain of ϵ is responsible for initial binding to F_1 and provides most of the binding energy. Without the C-terminal domain, partial inhibition by the ϵ N-terminal domain is due to enhanced ADP inhibition. The rapid effects of catalytic site ligands on conformational changes of F_1-bound ϵ suggest dynamic conformational and rotational mobility in F_1 that is paused near the catalytic dwell position.

ATP synthases play a key role in energy metabolism in most living organisms and achieve energy coupling as dual engine rotary nanomotors (1–3). The F-type ATP synthase of *Escherichia coli* (Fig. 1), a bacterial prototype, is composed of core subunits that all have homologs in the ATP synthases of mitochondria and chloroplasts (4). The membrane-embedded F_O complex (ab_2c_{10}) acts like a turbine to transport protons across the membrane, and the external F_1 complex ($\alpha_3\beta_3\gamma\delta\epsilon$) contains three cooperative catalytic sites for ATP synthesis or hydrolysis. The ring of *c*-subunits, with the critical proton transport sites, is the rotor complex of F_O and connects to the central rotor stalk of F_1, composed of γ and the N-terminal domain (NTD)[2] of ϵ. The three catalytic β subunits alternate with three α subunits to surround the upper half of the asymmetric rotor stalk of γ, and the δ-b_2 connection forms a peripheral stator stalk anchoring $\alpha_3\beta_3$ to the other stator subunit of F_O, *a*. *In vitro*, F_1 from eukaryotes and bacteria can be dissociated from F_O as a soluble, rotary motor ATPase, and these F_1-ATPases have been useful for both mechanistic studies and the determination of high resolution structures.

Despite general conservation between bacterial and mitochondrial ATP synthases, it has been demonstrated that bacterial ATP synthase can be an effective target for antibacterial treatment. It is the target of a novel class of compounds that are bactericidal for actively replicating and dormant mycobacteria (5, 6) and that show promising effects against multidrug-resistant tuberculosis in phase II clinical trials (7). However, the lead compound is only effective against a narrow spectrum of mycobacteria, and, because it targets the H^+-transporting sites of F_O, adapting this scaffold to target other pathogenic bacteria introduces a significant risk of cross-reaction with mitochondrial ATP synthase. Recently, our group determined the first crystal structure of a bacterial F_1-ATPase that is in an autoinhibited state mediated by the C-terminal domain (CTD) of its ϵ subunit (8). Inhibition by ϵ may serve regulatory roles in ATP synthases of bacteria (2, 9) and chloroplasts (10) but does not occur in mitochondrial ATP synthase, which has a distinct inhibitor protein (11). Recent studies confirmed that the bacterial ϵCTD inhibits ATP synthesis as well as hydrolysis (12, 13), indicating that ϵ inhibition may provide a new target for future development of antimicrobial drugs selective for bacteria. With that in mind, the current study focuses on improving our biochemical understanding of how the catalytic F_1 complex of *E. coli* ATP synthase is inhibited by ϵ.

* This work was supported, in whole or in part, by National Institutes of Health Grant R01GM083088 (to T. M. D.).
[S] This article contains supplemental Fig. S1 and Table S-I.
The atomic coordinates and structure factors (code 3OAA) have been deposited in the Protein Data Bank (http://wwpdb.org/).
[1] To whom correspondence should be addressed: Dept. of Biochemistry and Molecular Biology, SUNY Upstate Medical University, 750 E. Adams St., Syracuse, NY 13210. Tel.: 315-464-8711; Fax: 315-464-8750; E-mail: duncant@upstate.edu.

[2] The abbreviations used are: NTD, N-terminal domain; CTD, C-terminal domain; $ϵ_C$ and $ϵ_X$, compact and extended conformations of ϵ (Fig. 1); BLI, biolayer interferometry; Bap, biotin acceptor peptide; βME, 2-mercaptoethanol; DTNB, 5,5′-dithiobis(2-nitrobenzoate); MF_1, mitochondrial F_1-ATPase; TF_1, F_1-ATPase of thermophilic *Bacillus* sp. *PS3*; SM, single-molecule; H_6-ϵ, His_6-tagged ϵ; MBP, maltose-binding protein; AMPPNP, 5′-adenylyl-β,γ-imidodiphosphate.

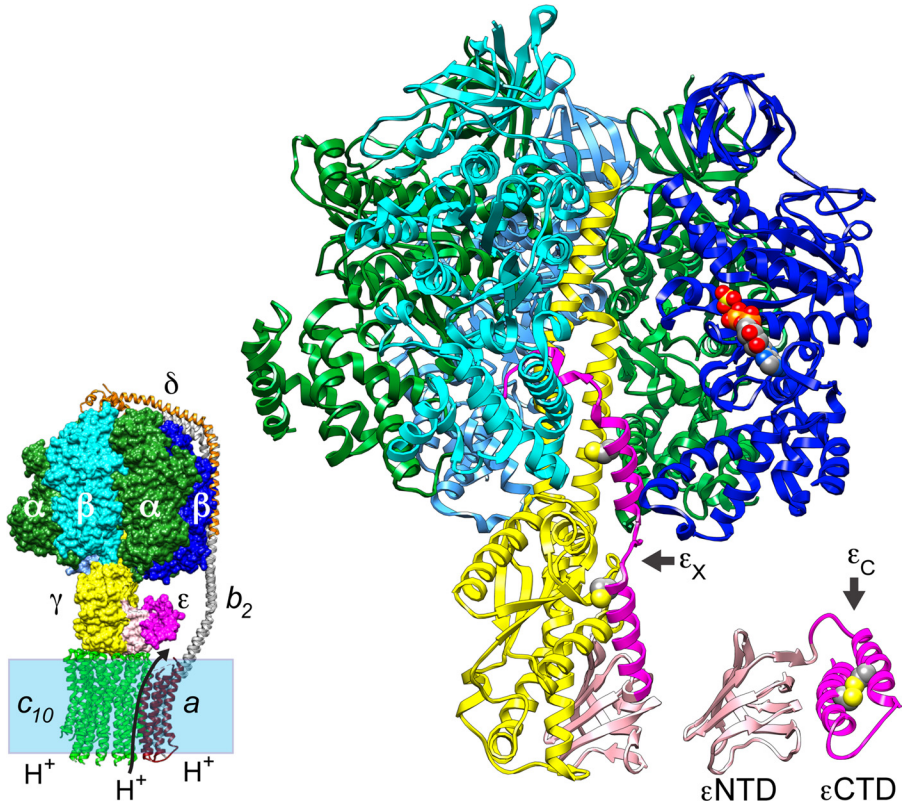

FIGURE 1. **Architecture of bacterial ATP synthase and alternate conformations of subunit ϵ.** The *smaller image* (*bottom left*) depicts the *E. coli* ATP synthase, with F_O subunits spanning the membrane bilayer (*shaded box*); the *arrow across* the bilayer indicates the direction of proton (H^+) transport during net ATP synthesis. F_O subunits (*ribbons*, *a* (*dark red*), b_2 (*gray*), and c_{10} (*green*)) and F_1 subunit δ (*orange ribbon*) are from a homology-modeled assembly (67). All other F_1 subunits are from determined structures and are surface-rendered in the F_OF_1 model but displayed as *ribbons* in the *magnified view* of *E. coli* F_1 (3α (green), 3β (*shades* of *blue*), γ (*yellow*), ϵNTD(1–87) (*light pink*), and ϵCTD(88–138) (*dark pink*)). The F_OF_1 model shows ϵ in the ϵ_C or compact conformation (Protein Data Bank entry 1BSN), docked to γ of EF_1-δ (Protein Data Bank entry 3OAA). The *magnified ribbon diagram* shows the ϵ-inhibited F_1-δ structure (Protein Data Bank entry 3OAA) and omits the foremost α subunit to reveal the extended conformation of ϵ (ϵ_X); for comparison, a *ribbon model* of the ϵ_C state is shown *offset* to the *right*. The *ribbon diagram* of each ϵ conformation shows space-filling side-chain atoms (*colored* by element) predicted *in silico* for mutations ϵA101C/L121C. Space-filling atoms are also shown for ADP and SO_4^{2-} on the one occupied catalytic β subunit (chain D). The molecular graphics were prepared with Chimera (81).

As shown in Fig. 1, the ϵ subunit has two domains. The ϵNTD, essential for the F_1 rotor connection to the *c*-ring in F_O (2, 9), is a β-sandwich fold and exhibits a similar conformation and association with γ in several structures of bacterial F_1 (8, 14) and mitochondrial F_1 (MF_1) (15, 16); essentially the same ϵNTD structure is also seen for isolated bacterial ϵ (17–19). However, the α-helical ϵCTD has been observed in dramatically different conformations (Fig. 1). A compact conformation (the ϵ_C state) has a coiled-coil between its two α-helices, and the second helix packs against the ϵNTD. The ϵ_C state has been observed for isolated bacterial ϵ (17–19) and in one bacterial F_1 structure (14). In structures of MF_1 (15) and MF_1·*c*-ring (20), the homolog of ϵ appears to be locked in the ϵ_C state by a mitochondria-specific subunit. *E. coli* ATP synthase can synthesize and hydrolyze ATP when ϵ is restricted to the ϵ_C state (21), in which the ϵCTD does not contact any F_1 subunits (Fig. 1, *left*). In contrast, in the recently determined structure of *E. coli* F_1 (Fig. 1) (8), an extended conformation of the ϵCTD (ϵ_X state) contacts five other subunits, and its terminal half is inserted into the central cavity of F_1. The position and subunit contacts of the ϵCTD within the *E. coli* F_1 structure correlate well with many biochemical studies of ϵ inhibition and interaction with other F_1 subunits (reviewed in Refs. 2 and 9). The extensive buried surface of the ϵCTD within the F_1 structure and its interactions with two catalytic β subunits suggest that this form of the enzyme represents an inactive state. This correlates with results of "single-molecule" (SM) studies of F_1 from *E. coli* (22) and other bacteria (23–26), showing that ϵ can induce or extend long "pauses" (seconds) during which γ does not rotate in the presence of substrate MgATP. Some SM studies concluded that ϵ inhibits by stabilizing or extending an ADP-induced inhibitory pause that occurs at the catalytic dwell (22, 24, 27), whereas another recently concluded that ADP- and ϵ-induced inhibitions are separate processes for cyanobacterial F_1 (25). Some studies also concluded that ϵ inhibition includes or is dominated by changes to one or more intrinsic kinetic steps along the catalytic pathway (12, 22, 28, 29). In the current study, we adapt an optical assay to directly measure the kinetics of binding and dissociation for *E. coli* F_1·ϵ and correlate these with inhibitory effects for wild type (WT) and mutant forms of ϵ. Our biochemical evidence confirms that inhibition by the CTD of ϵ initiates at the catalytic dwell but also shows that ϵ inhibition competes with formation of the ADP-inhibited state. Further, whereas ϵ inhibition initiates at the catalytic dwell, we also show that the balance between active and ϵ-inhibited states responds dynamically to changing nucleotide conditions.

EXPERIMENTAL PROCEDURES

Plasmid Constructs for Affinity-tagged E. coli ϵ Subunit—A plasmid described previously (30) (noted here as $pH_6\epsilon$) encodes a His_6-tagged ϵ (H_6-ϵ), with a tobacco etch virus protease cleavage site following the N-terminal His_6 tag. Site-directed mutagenesis was used to create the following mutations in H_6-ϵ. A pair of Cys mutations, ϵA101C/L121C, was created on $pH_6\epsilon$ using the QuikChange Multi site-directed mutagenesis kit (Stratagene) with primers 5′-CATGGAAGCGA-AACGT-AAGTGTGAAGAGCACATTAGGAG-3′ (ϵA101C) and 5′-GCTCAGGCGTCTGCGG-AATGCGCCAAAGCGATC-3′ (ϵL121C). H_6-ϵ that expresses only the ϵNTD (H_6-ϵ88stop; see Ref. 31) was created with the QuikChange-II XL kit (Stratagene) (forward primer, 5′-CAATTCGCGGCCAGTAAGTC-GACGAAGCG-3′). Plasmid pBKH2 was created to add a biotin acceptor peptide (Bap) before the N-terminal His_6 tag on H_6-ϵ. This $BapH_6$-ϵ has 49 residues before the native initial Met of ϵ, and tobacco etch virus cleavage would yield ϵ with three extra N-terminal residues (GAM). It was created with $pH_6\epsilon$ as a template, using PCR to generate a 514-bp amplicon with restriction sites added before (XhoI) and after (BamHI) the gene for H_6-ϵ (primers, 5′-CGACTCGAGCATGTCGTACTA-CCATCACC-3′ and 5′-CTCGGATCCTTACATCGCTTTTTTGGTCAAC-3′). Following cleavage with XhoI and BamHI, this amplicon was cloned into the same sites of pDW363 (32), replacing the *malE* gene, to create pBKH2. *BirA* (*E. coli* biotin holoenzyme synthetase) is co-expressed from pBKH2, allowing *in vivo* biotinylation of the biotin acceptor peptide on $BapH_6$-ϵ (32). $BapH_6$-ϵ expressed with ϵ88stop or ϵA101C/L121C had poor protein yields, so ϵ was also expressed as a fusion protein following an N-terminal maltose-binding protein (MBP), a cleavage site for PreScission protease (GE Healthcare), and the Bap tag. This MBP-Bap-ϵ has a 31-residue segment between MBP and the initial Met of ϵ, and after cleavage by PreScission protease, Bap-ϵ would retain a 25-residue N-terminal Bap tag. The vector for this construct, pMal-PPase, was derived from pMAL-c2e (New England Biolabs), with a PreScission protease cleavage sequence after *malE* (33), and an NdeI site was removed by cleavage and polymerase fill-in. The sequence encoding the Bap tag was PCR-amplified from pDW363, with flanking restriction sites before (StyI) and after (NdeI and BamHI) the Bap sequence (primers, 5′-CATCCCAAGGCTGGAGGCCTGAA-CGATATTTTC-3′ and 5′-CTCGGATCCCATATGGCCAC-CAGTGTCCTCGTG-3′). After cleavage with StyI and BamHI, this amplicon was inserted into StyI-BamHI sites of pMal-PPase to generate pMAL-PP-Bap. The *atpC* gene for WT ϵ was extracted from p3U (34) as a 625-bp NdeI-XbaI fragment and ligated into the same sites of pMAL-PP-Bap to create pBKH8, encoding a fusion protein of MBP-Bap-ϵ. Plasmids encoding MBP-Bap-ϵ with mutation ϵ88stop (pBKH9) or ϵA101C/L121C (pBKH10) were produced in the same way, but the NdeI-XbaI inserts were 799 bp (extra sequence downstream of *atpC*) because those mutant *atpC* genes had been passed through an intermediate vector.

Purification of Proteins—SDS-PAGE (35) (Bio-Rad Ready Gels, 12% or 4–15%) was used to analyze the purity of all protein preparations, with staining by SYPRO Orange (Invitrogen) and scanning on a Typhoon 9410 imager (GE Healthcare; 488-nm laser excitation, 526-nm SP emission filter). With gels to test for internal disulfide bonding in Bap-ϵA101C/L121C, concentrated gel sample buffer contained 0.5 mM *N*-ethylmaleimide instead of 2-mercaptoethanol (βME). Concentration of protein samples was determined by a modified Lowry assay (36). *E. coli* F_OF_1 was expressed, and F_1 was purified and depleted of subunit δ to form $F_1(-\delta)$ as described (8). $F_1(-\delta)$ was depleted of subunit ϵ by immunoaffinity chromatography (37), using three passages of 5–7 mg of $F_1-\delta$ through an anti-ϵ column (3 ml). At this stage, upon dilution and passage through two sequential centrifuge columns, luciferase assays (8) showed that $F_1(-\delta\epsilon)$ had the following endogenous nucleotide content (mol/mol $F_1(-\delta\epsilon)$ ± S.E. from four different samples): noncatalytic sites, 0.89 ± 0.13 ATP and 0.83 ± 0.04 ADP; catalytic sites, 0.1 ± 0.08 ATP and 1.49 ± 0.17 ADP.

Wild-type and mutant forms of H_6-ϵ were expressed in *E. coli* BL21 strain "T7 Express lysY" (New England Biolabs). H_6-ϵ was purified by affinity chromatography (column with 10 ml of TALON resin; Clontech) as described (30) but with ϵ-buffer at pH 7.5 (20 mM Tris-HCl, 100 mM NaCl, pH 7.5). After loading, the column was washed with buffer + 10 mM imidazole (10 column volumes) and buffer + 15 mM imidazole (4 column volumes) before elution with buffer + 100 mM imidazole (4 column volumes). Residual impurities were removed from H_6-ϵ by gel filtration (HiPrep-16/60, Sephacryl S100 HR, GE Healthcare Life Sciences), and pure H_6-ϵ was exchanged into ϵ-buffer + 10% (v/v) glycerol before storage at −80 °C. For some experiments, the His_6 tag was removed by treatment with 25 units/ml AcTEV™ protease (Life Technologies) protease for 6 h. The sample was then loaded on the TALON column, and untagged ϵ was collected in the flow-through, concentrated, and frozen in ϵ-buffer + 10% glycerol.

$BapH_6$-ϵ was expressed from pBKH2 in *E. coli* strain BL21. Cells were grown at 22 °C in a medium containing Luria broth, biotin (12.2 mg/liter), 4.5 M sorbitol, and 1 M betaine. Protein expression was induced by adding isopropyl 1-thio-β-D-galactopyranoside when the A_{595} reached 0.5. Cells were grown for 4 h after induction until the A_{595} reached ~1.0. $BapH_6$-ϵ was partially purified by TALON chromatography (as for H_6-ϵ). Fractionation with ammonium sulfate was then used; $BapH_6$-ϵ that precipitated between 25 and 55% saturation was dissolved in ϵ-buffer + 10% glycerol. Finally, $BapH_6$-ϵ was purified by gel filtration (Sephadex G-50 column, 44 cm × 1-cm diameter), concentrated by ultrafiltration (Vivaspin 6 concentrator, 5000 molecular weight cutoff), frozen in liquid N_2, and stored at −80 °C.

To express biotinylated MBP-Bap-ϵ mutants, *E. coli* strain DH5α was co-transformed with pBirAcm (which expresses BirA; Avidity (Aurora, CO)) and either pBKH9 (MBP-Bap-ϵ88stop) or pBKH10 (MBP-Bap-ϵA101C/L121C). Each strain was grown overnight at 37 °C in LB with ampicillin (100 μg/ml) and chloramphenicol (25 μg/ml). Overnight cultures were used to inoculate 2 liters of the same medium plus 0.4% glucose and 0.1 mM biotin. Cells were grown at 37 °C to A_{595} ~0.5, 0.4 mM isopropyl 1-thio-β-D-galactopyranoside was added to induce expression of MBP-Bap-ϵ and BirA, and growth continued for ~3.5 h at 37 °C. Cells were harvested by centrifugation and washed once with column buffer (20 mM Tris-HCl, pH 7.5, 200 mM NaCl, 1 mM EDTA). Cells

were lysed by sonication and centrifuged at 11,290 × *g* for 30 min, and the supernatant was passed through a 0.45-μm filter. This sample was mixed with 5 ml of amylose-agarose resin (New England Biolabs; pre-equilibrated with column buffer) and incubated at 4 °C, with rocking, for 2 h. The amylose resin was then sedimented (1000 × *g*, 3 min), the supernatant was discarded, and the resin was washed five times by centrifugation with 40 ml of column buffer + 5 mM βME. For the εA101C/L121C mutant, 5 mM βME was present throughout purification. The resin was incubated with 0.1 mg of PreScission Protease (4 °C, 3 h, in 15 ml of column buffer + 5 mM βME) to release Bap-ε, which was collected in the supernatant and in a subsequent wash of the resin with 10 ml of column buffer + 5 mM βME. Ultrafiltration (Vivaspin-20, 5000 molecular weight cut-off) was used to concentrate the Bap-ε from 25 to 1 ml and exchange it into ε buffer + 10% glycerol, including 1 mM βME for Bap-εA101C/L121C. Concentrated Bap-ε was frozen in liquid N_2 and stored at −80 °C. For some experiments, His_6- or Bap-tagged εA101C/L121C was treated with 5,5′-dithiobis(2-nitrobenzoate) (DTNB) to induce disulfide bonding between closely approaching cysteines (38). The sample was first passed through a Biogel P6 centrifuge column (39) (pre-equilibrated with 20 mM MOPS-Tris, 50 mM KCl, pH 8 (MTK8)) to remove βME. Tagged εA101C/L121C (~30 μM) was then incubated with 50 μM DTNB for 15 min or less at room temperature and passed through a second centrifuge column to remove excess DTNB.

ATPase Assays—A coupled enzyme assay (40) was used for continuous monitoring of ATP hydrolysis, and assays were done at 30 °C. Decrease in NADH concentration was monitored at 340 nm in a Hewlett-Packard 8453 spectrophotometer. The standard assay buffer was MTK8 supplemented with 1 mM phosphoenolpyruvate and 0.3 mM NADH. MgATP substrate was added from stock solutions of Mg acetate and Na_2ATP; concentrations and ratios of Mg^{2+}/ATP are noted for specific experiments. Pyruvate kinase (rabbit muscle, Roche Applied Science catalog number 109045) and lactate dehydrogenase (Porcine heart, Calbiochem catalog number 427211) were each present at 0.1 mg/ml in assays with excess Mg^{2+} *versus* ATP; for assays with excess ATP *versus* Mg^{2+}, pyruvate kinase was 0.2 mg/ml. In some assays, hydrolysis of GTP was measured rather than ATP. For assays measuring inhibition by ε, BSA (fatty-acid free) was added at 0.5 mg/ml, EDTA was added to 0.1 mM, and $F_1(-\delta\varepsilon)$, ε, and ATP were added to final concentrations and preincubated at 30 °C for 10 min; the assay was initiated by adding magnesium acetate from a concentrated stock and mixing. Hydrolysis rates were measured at steady state, typically 12–15 min after adding Mg^{2+}. For each data set varying ε concentration, a fixed concentration of $F_1(-\delta\varepsilon)$ was used (F_T = 0.6 or 1.2 nM), and hydrolysis rates were fit by nonlinear regression (Prism, GraphPad, Inc.) to the following equation,

$$A_i = A_0 - (A_0 - A_e)\cdot\left(\frac{K_I + \varepsilon_i + F_T - \sqrt{(K_I + \varepsilon_i + F_T)^2 - 4\cdot\varepsilon_i\cdot F_T}}{2\cdot F_T}\right) \quad \text{(Eq. 1)}$$

where A_0 is the rate measured for $F_1(-\delta\varepsilon)$ alone, A_i is the rate measured at each ε concentration, ε_i, A_e is the rate fitted for ε-saturated $F_1(-\delta\varepsilon)$, and K_I is the apparent dissociation constant fitted for $F_1{\cdot}\varepsilon$ binding. For assays of inhibition by azide, magnesium acetate, ATP, sodium azide, and ε (if any) were added first, and the assay was initiated by adding $F_1(-\delta\varepsilon)$ from a concentrated stock; steady-state rates were measured as above.

Kinetic Assays of Binding and Dissociation between $F_1(-\delta\varepsilon)$ and Biotinylated ε, Using Biolayer Interferometry (BLI)—An Octet-RED system and streptavidin-coated sensors (FortéBio, SA biosensors, catalog number 18-5019) were used to monitor BLI kinetics of protein-protein binding and dissociation, analogous to surface plasmon resonance techniques (41). MTK8 buffer included 0.5 mg/ml BSA to minimize nonspecific binding of proteins to the sensors and as carrier protein for nanomolar dilutions of $F_1(-\delta\varepsilon)$ or ε. All steps were done at 30 °C, with each sensor stirred in 0.2 ml of sample at 1000 rpm and a standard measurement rate of 5 s^{-1}. Wild-type or mutant forms of biotinylated ε ($BapH_6$-ε, or Bap-ε after cleavage from MBP-Bap-ε) were immobilized on SA biosensors. Levels of *in vivo* biotinylation varied between ε samples, so preliminary BLI titrations were done for each biotinylated ε to determine the Bap-ε concentration and loading time needed for optimal BLI kinetic responses in subsequent binding of $F_1(-\delta\varepsilon)$ to the ε-loaded sensors. Minimal loading of ε was found to be favorable for kinetic responses to $F_1(-\delta\varepsilon)$ binding, so most subsequent experiments loaded biotinylated ε to yield 0.2–0.4 nm of BLI signal per sensor. Use of reference sensors with immobilized biotinylated ε but without added $F_1(-\delta\varepsilon)$ confirmed that added ligands (nucleotides, Mg^{2+}, EDTA, and azide) did not alter the BLI signal for immobilized ε. To correct for BLI baseline drift and minimal nonspecific binding of $F_1(-\delta\varepsilon)$ to sensors, all BLI experiments included one or more reference sensors in parallel for which biotinylated ε was omitted from the ε-loading step, but $F_1(-\delta\varepsilon)$ was included in the association step, usually at the highest concentration of $F_1(-\delta\varepsilon)$ used for each experiment. FortéBio's analysis software (version 6.4) was used for reference subtraction, Savitsky-Golay filtering, and global fitting of kinetic rates for $F_1{\cdot}\varepsilon$ binding and dissociation.

RESULTS

Inhibition of E. coli F_1 by ε with and without the εCTD—Upon *in vitro* dissociation of *E. coli* F_1 from the membrane, ε becomes more inhibitory but can dissociate upon dilution of F_1, relieving inhibition of F_1-ATPase activity (2). For most experiments in this study, we used F_1 that was depleted of δ and ε subunits, or $F_1(-\delta\varepsilon)$. The stator subunit δ does not significantly affect F_1-ATPase activity (42) but was removed because its dissociation from F_1 could interfere with assays below for $F_1{\cdot}\varepsilon$ binding and dissociation. Fig. 2 compares inhibition of $F_1(-\delta\varepsilon)$ by WT and mutant forms of H_6-ε, and Table 1 summarizes the inhibition parameters from regression curves of Fig. 2 and an additional data set. As noted before (30), the N-terminal His_6 tag on WT ε did not significantly alter inhibition compared with WT ε that had the tag removed (Table 1). Also, inhibition was not altered by the N-terminal Bap tag added to ε (WT and mutants) for kinetic assays of $F_1{\cdot}\varepsilon$ binding and dissociation (not shown). For WT ε, values for the inhibitory constant K_I and residual activity of ε-saturated F_1 agree with earlier estimates (29, 43).

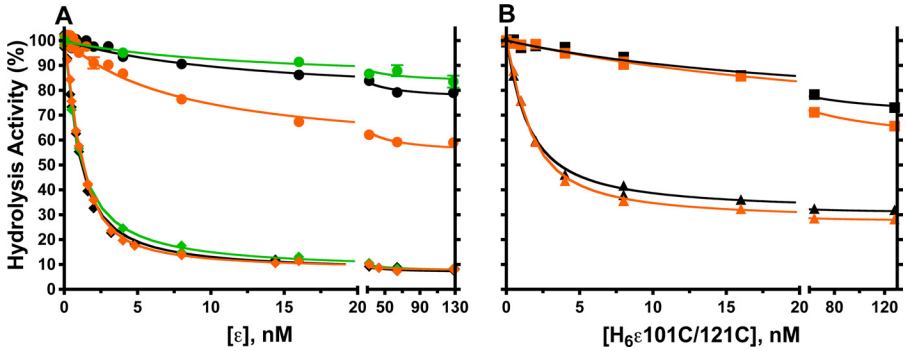

FIGURE 2. **Effects of truncating or cross-linking the ϵCTD on inhibition of $F_1(-\delta\epsilon)$.** *A*, $F_1(-\delta\epsilon)$ was preincubated for 10 min with 0.1 mM EDTA and ATP (*black* and *orange symbols*) or GTP (*green symbols*) and the indicated concentrations of wild-type H_6-ϵ (♦) or H_6-ϵ88stop (●). Hydrolysis was initiated by adding magnesium acetate. Final concentrations of added ligands were as follows: 2:1 mM ATP/Mg^{2+} (black); 1:2 mM ATP/Mg^{2+} (*orange*); 1:2 mM GTP/Mg^{2+} (*green*). *B*, ATPase assays as for *A*, but H_6-ϵA101C/L121C was used with 1 mM DTT present (▲) or with an ϵA101C–L121C disulfide bond (■). See "Experimental Procedures" for assay details and regression analysis. With H_6-ϵ88stop, data points are averages from three (ATP) or two (GTP) experiments, and standard *error bars* are included but are smaller than the *symbols* for most points. Results of regression analyses for these and for a data set with untagged WT ϵ are summarized in Table 1.

TABLE 1

Inhibition of $F_1(-\delta\epsilon)$ by variants of subunit ϵ

Results of nonlinear regression for data shown in Fig. 2 and a data set with untagged WT ϵ. Equation 1 was used (see "Experimental Procedures").

ϵ	NTP/Mg^{2+} ratio	Activity of $F_1(-\delta\epsilon)$ $(A_0)^a$	Activity of ϵ-saturated F_1 $(A_e/A_0)^b$ ± S.E.^{c}	K_I ± S.E.^{c}
	mM	*μmol min^{-1} mg^{-1}*	*%*	*nM*
Wild type	ATP 2:1	78	7.9 ± 0.6	0.49 ± 0.02
Wild-type H_6-ϵ	ATP 2:1	78	6.8 ± 0.8	0.67 ± 0.04
	ATP 1:2	37	7.9 ± 0.5	0.46 ± 0.02
	GTP 1:2	94	7.3 ± 0.7	0.87 ± 0.04
H_6-ϵ88stop	ATP 2:1	73	76.3 ± 1.2	12.4 ± 1.9
	ATP 1:2	36	54.6 ± 1.4	7.2 ± 0.8
	GTP 1:2	95	84 ± 2.0	13 ± 7
H_6-ϵ101C/121C, + 1 mM DTT	ATP 2:1	80	31 ± 1	1.2 ± 0.1
	ATP 1:2	41	27 ± 1	0.98 ± 0.06
H_6-ϵ101C/121C, disulfide-bonded	ATP 2:1	80	69 ± 2	23 ± 3.7
	ATP 1:2	38	58 ± 1	31 ± 2

[a] Hydrolysis activity units are μmol·min^{-1}·mg^{-1} $F_1(-\delta\epsilon)$.
[b] Activity of ϵ-saturated $F_1(-\delta\epsilon)$, A_e, is listed as a percentage of A_0, the measured activity of $F_1(-\delta\epsilon)$ alone.
[c] S.E., standard error from nonlinear regression.

We obtained nearly the same parameters for ϵ inhibition in assays with ATP $< K_m$ (not shown), consistent with noncompetitive inhibition by ϵ *versus* ATP (29, 44). We also show that the >90% inhibition by saturating WT ϵ was unaffected by excess Mg^{2+} (Fig. 2*A*), although $F_1(-\delta\epsilon)$ alone was inhibited >50% by 1 mM excess Mg^{2+} (Table 1).

To test for inhibition by ϵ lacking its CTD, we used ϵ88stop, one of the largest C-terminal deletions that still allows assembly of F_OF_1 that is functionally coupled, both *in vivo* and *in vitro* (31). In Fig. 1, both conformations of ϵ are *colored darker* for the C-terminal region that is absent in ϵ88stop. As shown in Fig. 2*A*, H_6-ϵ88stop caused much less inhibition than WT H_6-ϵ and had a >15-fold larger K_I, confirming that the ϵCTD is responsible for the majority of inhibition. However, unlike WT H_6-ϵ, the maximal extent of inhibition by H_6-ϵ88stop almost doubled to ~45% in the presence of excess free Mg^{2+}. Inhibitory effects of free Mg^{2+} are linked to inhibitory MgADP bound at a catalytic site on F_1 from *E. coli* (45, 46), from other bacteria (47), from mitochondria (48, 49) and chloroplasts (50, 51), and hydrolysis of GTP is less sensitive to this type of inhibition (45, 48, 52). For example, with 1 mM excess Mg^{2+}, GTPase turnover by $F_1(-\delta\epsilon)$ is ~2.5-fold faster than ATPase (Table 1). We show that WT H_6-ϵ exhibits similar high affinity inhibition for GTPase and ATPase (Fig. 2*A* and Table 1). However, H_6-ϵ88stop inhibited GTPase much less, ~16% maximal, both with excess free Mg^{2+} present (Fig. 2*A*) and without it (not shown). Thus, observed partial inhibition of ATPase by the ϵNTD is largely due to increased MgADP inhibition in the absence of the ϵCTD. This can also explain why ϵ truncated after ϵ94 (with only about half of the first helix remaining) inhibited *E. coli* F_1 ~50% because the assays contained 2 mM excess free Mg^{2+} (53). The effects of the ϵNTD are distinct from the >90% inhibition caused by the ϵCTD of intact WT ϵ, which is not sensitive to the effects of excess Mg^{2+}.

As an alternative to removing the ϵCTD, we also used the ϵA101C/L121C mutant (21).[3] This cysteine pair can form a disulfide bond in nearly 100% yield (Fig. 3) that cross-links the two α-helices of the ϵCTD in the ϵ_C conformation, preventing ϵ

[3] The original study with ϵA101C/L121C (21) showed that an ϵA101C–L121C disulfide bond could be formed in membrane-bound F_OF_1 but did not appear to alter ATPase activity. We tested membranes expressing F_OF_1 with ϵA101C/L121C and showed that removing DTT from the sample activated ATPase 2-fold; this is the same activation seen originally (21) after inducing a disulfide between the ϵCTD and ϵNTD (ϵM49C-A126C). We believe that their ATPase assays did not include reductant for the non-oxidized sample of F_OF_1 + ϵA101C/L121C and that the disulfide formed quickly and spontaneously, as we have observed (Fig. 3). Thus, they would not have observed activation of ATPase by oxidation of ϵA101C–L121C if the disulfide had also formed in the non-oxidized sample.

from switching to the ϵ_X conformation (see Fig. 1). As shown in Fig. 2*B*, this disulfide linkage prevented high affinity inhibition of $F_1(-\delta\epsilon)$ as effectively as removing the εCTD. However, the partial inhibition observed was less sensitive to excess free Mg^{2+} than with H_6-ε88stop; this suggests that εCTD/εNTD interactions in the ϵ_C state can influence interactions of εNTD with γ that alter catalytic behavior. With DTT present to prevent the disulfide bond, H_6-εA101C/L121C could access the ϵ_X state and showed high affinity inhibition (K_I ~1 nM), similar to that with WT H_6-ε (K_I ~0.5 nM). However, the activity of F_1 saturated with reduced H_6-εA101C/L121C was 4-fold greater than with WT H_6-ε. In the structure of ε-inhibited F_1 (8), εLeu-121 is in a coiled-coil interface with the γ N-terminal helix, and the εL121C mutation probably perturbs this interface, favoring more F_1 complexes in the active state on average. This supports the concept that, with ε-saturated F_1, the residual ATPase activity (7–8% with WT ε) is due to the time-averaged fraction of F_1 complexes in which ε is not in the inhibitory ϵ_X conformation.

Kinetics of F_1·ε Binding and Dissociation, Assayed by BLI—In preliminary assays, H_6-ε was loaded on BLI sensors coated with Ni^{2+}-nitrilotriacetic acid, but slow dissociation of WT H_6-ε from the sensors prevented accurate measures of the slow dissociation rate of F_1 from WT H_6-ε. To achieve more stable and specific attachment of ε to the sensor surface, ε was engineered with an N-terminal Bap tag, so that a specific lysine could be biotinylated *in vivo* (32). Biotinylated Bap-ε could be stably bound to streptavidin-coated sensors (supplemental Fig. S1), and BLI was then used to measure binding and dissociation kinetics of $F_1(-\delta\epsilon)$. For each Bap-ε variant, 4–7 sensors were used in parallel, with $F_1(-\delta\epsilon)$ concentrations varied ≥10-fold

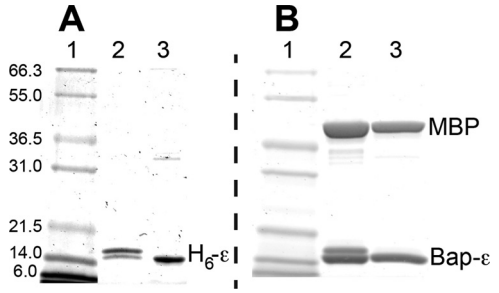

FIGURE 3. **SDS-PAGE analysis of disulfide bond formation with εA101C/L121C.** Samples were applied to 12% SDS-PAGE under non-reducing conditions. *Lane 1* of each gel, molecular mass markers (approximate kDa noted for gel A). *Gel A*, samples of H_6εA101C/L121C (1 μg/*lane*) were taken immediately after DTT was removed from the sample by centrifuge column (*lane 2*) or after 2 min of reaction with 50 μM DTNB (*lane 3*). *Gel B*, samples of (MBP-cleaved) Bap-ε (5 μg/*lane*) were taken after removing DTT as above (*lane 2*) or after reaction with 50 μM DTNB for 15 min (*lane 3*). With 2-mercaptoethanol in the gel sample buffer (not shown), each εA101C/L121C migrated only at the upper band position (above 14 kDa standard), confirming that the lower band seen here was a faster migrating band due to the internal εA101C–L121C disulfide bond.

in the association samples, and association/dissociation kinetics were fit globally to determine the rate constants (Table 2). K_D values derived from the rate constants correlate well with inhibitory K_I values (Table 1) for WT ε, ε88stop, and disulfide-bonded εA101C/L121C. Representative kinetics for binding/dissociation of $F_1(-\delta\epsilon)$ with sensors containing WT ε or ε88stop are shown in Fig. 4. The εCTD did not significantly alter the association rate, indicating that only εNTD/γ interactions are involved in initial F_1·ε binding. In contrast, removing the εCTD (Fig. 4) or preventing it from adopting the ϵ_X state (disulfide-bonded εA101C/L121C) increased the dissociation rate by ≥80-fold (Table 2). For sensors loaded with biotinylated WT BapH_6-ε, only a small fraction of bound $F_1(-\delta\epsilon)$ could be observed to dissociate in buffer only (Fig. 4), but results presented below show that essentially all $F_1(-\delta\epsilon)$ on the sensor is reversibly bound. Additional assays (not shown) included excess, non-biotinylated WT H_6-ε in the dissociation phase and confirmed that the observed, slow dissociation rate was not due to rebinding of $F_1(-\delta\epsilon)$ to the sensor. Thus, the much slower dissociation of $F_1(-\delta\epsilon)$/WT-ε is probably due to strong bias of bound WT ε to reside in the ϵ_X state, with the εCTD buried within F_1. However, from the K_D values (Table 2), note that the εCTD contributes only ~20% to the net free energy for F_1·ε binding ($\Delta\Delta G$, −10 or −12 kJ/mol for WT ε *versus* ε88stop or disulfide-bonded εA101C–L121C, respectively). This does not mean the ϵ_X state of εCTD has only weak interactions with other F_1 subunits; rather, the small contribution to net binding energy is probably due to the loss of favorable interactions between γ and $\alpha_3\beta_3$ that are blocked by insertion of the εCTD.

Effects of F_1 Ligands (Mg^{2+}, Nucleotides, P_i) on Conformational Bias of Bound, Full-length ε—From the crystal structure of ε-inhibited F_1 (8), the extensive surface area of εCTD that is buried within the central cavity of F_1 suggests that the ϵ_X state of ε does not directly dissociate from F_1; the slow dissociation observed in Fig. 4 probably occurs due to dynamic transition of ε between ϵ_X and conformations like ϵ_C in which the εCTD is outside of the central rotor cavity. Thus, factors that influence the fraction of F_1 complexes with ε in the ϵ_X state should alter the kinetics of F_1·ε dissociation. To show that the conformation of ε on *E. coli* F_1 and F_OF_1 can be influenced by nucleotides and other ligands that interact with catalytic sites, early studies used static assays, such as the capacity to form a β-ε cross-link; cross-linking of β-ε was minimized by non-hydrolysis conditions, such as ATP/EDTA or MgAMPPNP but maximized by post-hydrolysis conditions (MgADP/P_i) (54, 55). The β-ε cross-linking residues (56) are within hydrogen-bonding distance in the structure of ε-inhibited F_1 but should be at least 35 Å apart with ε in the ϵ_C state (8). Here, we use the BLI assay for F_1·ε binding/dissociation for more dynamic analyses of how different ligands

TABLE 2
Binding/dissociation rates and K_D values for $F_1(-\delta\epsilon)$ with variants of subunit ε

Biotinylated ε	k_a ± S.E.[a]	k_d ± S.E.[a]	K_D
	$M^{-1}\,s^{-1}$	s^{-1}	nM
Wild type	$2.0 \times 10^5 \pm 0.1\%$	$4.8 \times 10^{-5} \pm 0.1\%$	0.24
Wild type, +1 mM EDTA/ATP	$2.3 \times 10^5 \pm 0.1\%$	$4.1 \times 10^{-3} \pm 0.1\%$	17
ε88stop	$3.1 \times 10^5 \pm 0.6\%$	$3.8 \times 10^{-3} \pm 0.4\%$	12.2
εA101C/L121C, disulfide-bonded	$2.1 \times 10^5 \pm 0.3\%$	$6.6 \times 10^{-3} \pm 0.2\%$	32

[a] S.E., standard error from global fitting analysis (presented as a percentage of the parameter's value).

may shift the conformation of F_1-bound ϵ between the ϵ_X state and other conformations of the ϵCTD that allow faster F_1·ϵ dissociation. In control assays (not shown), the various ligands tested did not alter the rate at which $F_1(-\delta\epsilon)$ dissociated from biotinylated ϵ88stop, confirming that the ligand effects are specific to the ϵCTD of WT ϵ. $F_1(-\delta\epsilon)$ was bound in parallel to multiple sensors with biotinylated WT ϵ, and Fig. 5 shows dissociation of $F_1(-\delta\epsilon)$ when sensors were exposed to different ligands. For Fig. 5*A*, $F_1(-\delta\epsilon)$ was bound to all sensors in MTK8 buffer + BSA, and dissociation in this buffer was slow (Fig. 5*A*, *curve 4*, $\sim 5.4 \times 10^{-5}\ s^{-1} \pm 0.2\%$). This is consistent with access to the ϵ_X state when F_1 is in a post-hydrolysis conformation because isolated $F_1(-\delta\epsilon)$ retained ~1.5 ADP (mol/mol) but negligible ATP at catalytic sites (see "Experimental Procedures"). Added MgADP/P_i (Fig. 5*A*, *curve 5*) appeared to stabilize the ϵ_X state, consistent with prior β-ϵ cross-linking results (55). However, a similar effect was achieved by adding only Mg^{2+} and P_i (Fig. 5*A*, *curve 6*), suggesting that the endogenous ADP in isolated $F_1(-\delta\epsilon)$ was sufficient to stabilize the ϵ_X state upon the addition of Mg^{2+} and P_i. The importance of P_i in stabilizing this state (55) was also observed here because MgADP alone (Fig. 5*A*, *curve 2*) allowed a significant fraction of F_1 to dissociate faster.

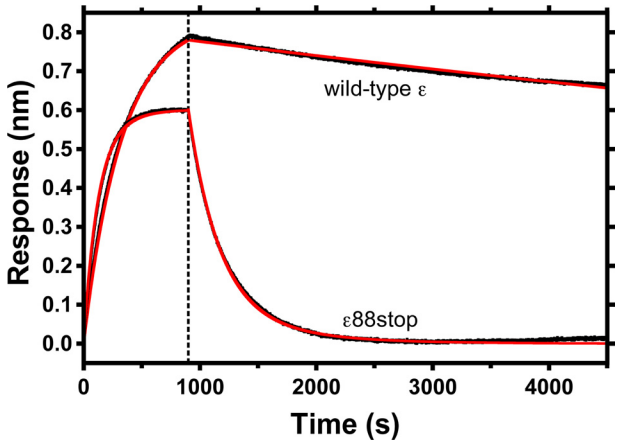

FIGURE 4. **Binding and dissociation kinetics for $F_1(-\delta\epsilon)$ and sensor-bound biotinylated ϵ, with or without ϵCTD.** Biotinylated Bap-ϵ (wild type or ϵ88stop, as noted) was loaded onto streptavidin biosensors. At time 0, each sensor was transferred from buffer alone to a sample containing 15 nM $F_1(-\delta\epsilon)$. After 900 s (*vertical dashed line*), each sensor was moved into buffer without $F_1(-\delta\epsilon)$. *Black lines*, experimental data; *red lines*, the kinetic fits for each ϵ, from global regression of kinetic data at varied concentrations of $F_1(-\delta\epsilon)$. Kinetic parameters and K_D values derived from the fittings are summarized in Table 2.

In contrast to slow F_1·ϵ dissociation under post-hydrolysis conditions, the addition of 1 mM ATP/EDTA caused ~94% of F_1·ϵ to dissociate ~80-fold faster (Fig. 5*A*, *curve 1*, $4.2 \times 10^{-3}\ s^{-1} \pm 0.1\%$) and with <3-s transition to faster dissociation (Fig. 5*C*). This effect is due to ATP because EDTA alone had a minimal effect on F_1 dissociation from immobilized WT ϵ (not shown). Further, by including 1 mM ATP/EDTA during association and dissociation phases, global analysis of F_1·ϵ binding/dissociation shows that ATP/EDTA did not alter the F_1·ϵ binding rate but gave a dissociation rate and K_D similar to values for ϵ88stop (Table 2). The presence of nonhydrolyzable MgAMPPNP (2:1 mM) during the dissociation phase (not shown) also accelerated F_1·ϵ dissociation, indicating that nucleotide binding alone is sufficient to shift F_1 to a conformation that does not allow the ϵCTD to insert into F_1 and form the ϵ_X state. Also, the ability of MgADP/P_i to stabilize the inhibitory state of ϵ was readily reversible; even when $F_1(-\delta\epsilon)$ was bound to

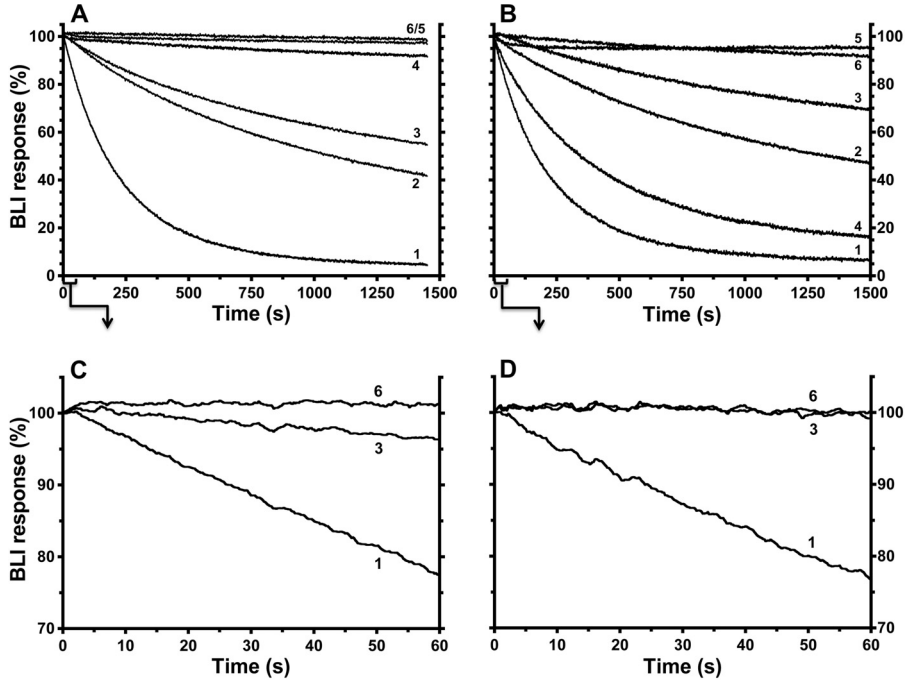

FIGURE 5. **Effects of other ligands on dissociation of F_1 from sensor-bound wild-type ϵ.** $F_1(-\delta\epsilon)$ (50 nM) was incubated for ~10 min in MTK8 + BSA buffer only (*A*) or plus 1 mM ATP/EDTA (*B*) and then incubated with BLI sensors containing WT $BapH_6$-ϵ to equilibrate F_1·ϵ binding. Signals for bound $F_1(-\delta\epsilon)$ varied slightly between sensors (6–9%), so data were normalized for display. Results show the kinetics of $F_1(-\delta\epsilon)$ dissociation upon moving sensors into buffer with different ligands. *C* and *D*, selected results from *A* and *B*, respectively, for the initial 60 s of dissociation. When present, Mg^{2+} was at 2 mM; all other ligands were 1 mM. *Curve 1*, ATP/EDTA; *curve 2*, MgADP; *curve 3*, MgATP; *curve 4*, buffer only; *curve 5*, MgADP/P_i; *curve 6*, Mg^{2+}/P_i.

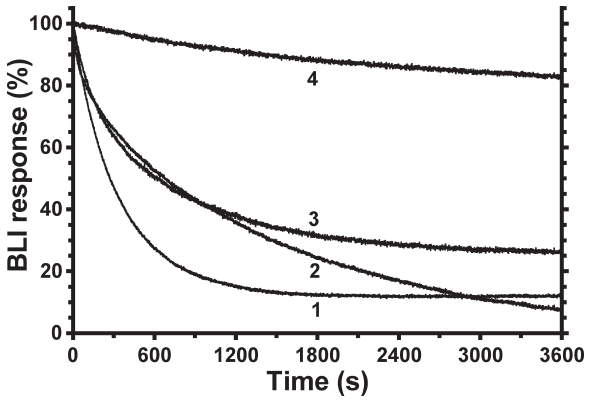

FIGURE 6. **Contrasting effects of Mg^{2+}/P_i on F_1·ϵ dissociation after preincubating F_1 with ATP/EDTA or MgAMPPNP.** $F_1(-\delta\epsilon)$ (50 nM) was incubated ~10 min in MTK8 buffer containing 2:1 mM MgAMPPNP (*curves 1–3*) or 1 mM ATP/EDTA (*curve 4*) and incubated with BLI sensors containing WT $BapH_6$-ϵ. BLI signals for bound $F_1(-\delta\epsilon)$ were normalized as in Fig. 5. Kinetics of F_1 dissociation were monitored in the presence of 2:1 mM MgAMPPNP (curve 1), buffer only (*curve 2*), or 2:1 mM Mg^{2+}/P_i (*curves 3* and *4*).

WT ϵ/sensors for 45 min with MgADP/P_i present, switching the sensors to buffer with MgAMPPNP immediately caused >90% of $F_1(-\delta\epsilon)$ to dissociate at the faster rate (not shown; $3.7 \times 10^{-3}\ s^{-1} \pm 0.1\%$).

For the experiment in Fig. 5*B*, $F_1(-\delta\epsilon)$ was bound to immobilized WT ϵ in the presence of 1 mM ATP/EDTA, so that most F_1·ϵ complexes would not have ϵ in the slowly dissociating ϵ_X state at the time the sensors were moved to dissociation wells. As expected, F_1 dissociation was fast with ATP/EDTA present (Fig. 5*B*, *curve 1*). With buffer only (Fig. 5*B*, *curve 4*), most F_1 still dissociated fast. This could indicate that ATP bound during the F_1·ϵ association phase dissociated slowly or that endogenous ADP had dissociated from F_1 during the association phase due to the ATP/EDTA present. MgADP alone (Fig. 5*B*, *curve 2*) slowed dissociation of most F_1, but MgADP/P_i (Fig. 5*B*, *curve 5*) or Mg^{2+}/P_i (Fig. 5*B*, *curve 6*) effectively reversed the ATP/EDTA effect so that almost all F_1 dissociated very slowly. Mg^{2+} was essential for this effect; without it, F_1 dissociation in the presence of 1 mM P_i (not shown) was nearly identical to that in buffer alone (Fig. 5*B*, *curve 4*). The effect of Mg^{2+} was enhanced by submillimolar P_i (not shown, $K_{½}$ ~0.2 mM P_i), similar to how P_i enhanced MgADP protection of F_1-bound ϵ from trypsin (55).

With Mg^{2+}/P_i, there was no apparent lag in reverting F_1·ϵ to slow dissociation (Fig. 5*D*, *curve 6*). This suggested that, after F_1·ϵ association with ATP/EDTA present, rapid reversion by Mg^{2+}/P_i to slow F_1·ϵ dissociation required hydrolysis of ATP that remained bound at a catalytic site. In the dissociation step, added Mg^{2+} could complex with the bound ATP, and hydrolysis would return F_1 to the catalytic dwell step, at which insertion of the ϵCTD into the central cavity appears to occur. The bound MgADP/P_i present would then stabilize F_1 with ϵ in the ϵ_X state. The experiment shown in Fig. 6 tested this possibility. With non-hydrolyzable MgAMPPNP present during F_1·ϵ association, dissociation of most F_1·ϵ was fast in the presence of MgAMPPNP (Fig. 6, *curve 1*) or in buffer alone (Fig. 6, *curve 2*), similar to the effects of ATP/EDTA in Fig. 5*B*. However, with MgAMPPNP present during association, inclusion of Mg^{2+}/P_i during dissociation failed to prevent fast dissociation of most F_1 (Fig. 6, *curve 3*), in contrast to the parallel control with ATP/EDTA in association (Fig. 6, *curve 4*). These results indicate that, with catalytic nucleotide bound in a prehydrolysis state, the rotary conformation of F_1 does not allow insertion of the ϵCTD into the central rotor cavity, but hydrolysis at the catalytic dwell allows the ϵCTD access to insert and form the ϵ_X state.

In the experiments of Fig. 4, hydrolysis conditions had complex effects on F_1·ϵ dissociation. With or without ATP/EDTA during F_1·ϵ binding, MgATP in the dissociation phase (*curve 3*) induced a small or negligible rate of F_1·ϵ dissociation during the initial 60 s (Fig. 5, *C* and *D*). Comparable with conditions for Fig. 5*B*, assays for ϵ inhibition of F_1-ATPase (Fig. 2) included an ATP/EDTA preincubation, and ϵ-saturated F_1 had initial ATPase activity (1–2 min, not shown) that was ~85% of the steady-state, inhibited rate. Thus, compared with fast F_1 dissociation in the continued presence of ATP/EDTA, hydrolysis of MgATP initially reverted F_1·ϵ complexes to slow dissociation, rapidly re-establishing the bias toward the inhibitory ϵ_X state (Fig. 5*D*, *curves 1* and *3*). This is consistent with noncompetitive inhibition of ϵ *versus* MgATP and, combined with other results above, indicates that ϵ accesses the inhibitory ϵ_X state following hydrolysis at the catalytic dwell step. On the longer time scale of Fig. 5 (*A* and *B*), hydrolysis conditions increased the dissociation rate for a fraction of F_1·ϵ complexes. As indicated by other experiments below, this slow effect on F_1·ϵ dissociation is probably due to gradual competitive transition of some active complexes to the ADP-inhibited state, which favors faster dissociation of ϵ. The fast dissociating fraction was substantially smaller for F_1·ϵ complexes formed in the presence of ATP/EDTA (Fig. 5*B*), probably because the ATP/EDTA preincubation minimizes initial inhibition (not shown) due to ADP-inhibited complexes.

Inhibition of $F_1(-\delta\epsilon)$ by Azide and the ϵCTD Are Competing Processes—The above results support prior SM mechanics studies (22–24, 26) that concluded that ϵ inhibition pauses rotation at the catalytic dwell position. In the absence of ϵ, long pauses at the catalytic dwell have been documented and attributed to inhibitory MgADP (57, 58). However, there have been conflicting conclusions about the relationship between inhibitory MgADP and ϵ inhibition for F_1 of different bacterial species (22, 24, 25, 27). We investigated this by testing interactions between ϵ inhibition and inhibition by sodium azide, which acts by stabilizing the MgADP-inhibited state (45, 59–61). We first tested inhibition of $F_1(-\delta\epsilon)$ by azide, with or without excess WT or mutant forms of H_6-ϵ present. Inhibition of $F_1(-\delta\epsilon)$ alone showed a K_I of ~5 μM azide, whether assays were done with 2:1 mM Mg/ATP (Fig. 7) or with 1:2 mM Mg/ATP (not shown). Thus, for *E. coli* F_1, azide inhibition is separated from the step that confers sensitivity to inhibition by excess free Mg^{2+}. The K_I for azide was not altered by bound H_6-ϵ mutants that could not access the ϵ_X state due to truncation (ϵ88stop) or disulfide bonding (ϵA101C–L121C). The presence of 100 nM WT ϵ reduced the activity of $F_1(-\delta\epsilon)$ ~10-fold, but the residual activity was still inhibited by excess azide. However, bound WT H_6-ϵ increased the K_I for azide ~5-fold (Fig. 7). Also, saturating $F_1(-\delta\epsilon)$ with reduced H_6-ϵA101C/L121C, which was less inhibitory than WT H_6-ϵ, yielded an intermediate K_I value for azide

inhibition. These results indicate that forming the inhibitory ϵ_X state competes with azide's capacity to inhibit F_1-ATPase. To test whether azide also competed with formation of the ϵ-inhibited state, $F_1(-\delta\epsilon)$ was bound to immobilized WT $BapH_6$-ϵ in buffer alone, and F_1·ϵ dissociation was measured under hydrolysis conditions with varied concentrations of azide (Fig. 8*A*). Increasing azide concentrations caused greater fractions of F_1·ϵ to dissociate at a faster rate, and the hyperbolic dependence on azide (Fig. 8*B*) yielded a $K_{½}$ of ~14 μM, comparable with the mid-range of K_I values for azide inhibition with or without WT H_6-ϵ (Fig. 6). Taken together, the results of Figs. 7 and 8 show competition between (i) the ability of the ϵCTD to insert, forming the inhibitory ϵ_X state, and (ii) the ability of azide to bind to and stabilize the MgADP-inhibited state of F_1.

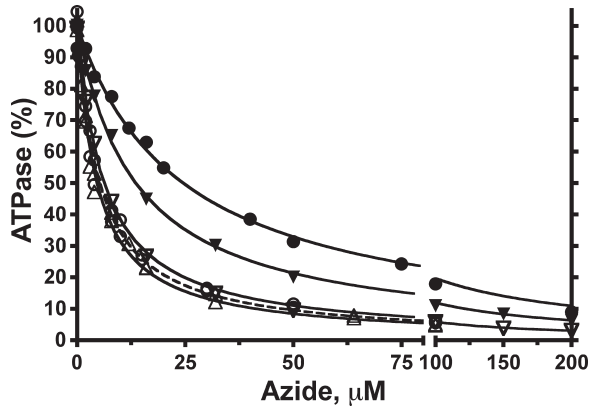

FIGURE 7. **Effects of excess ϵ variants on inhibition of F_1-ATPase by azide.** Steady-state ATPase rates were measured for $F_1(-\delta\epsilon)$ in the presence of varied concentrations of sodium azide. Assays were done in the absence of ϵ or in the presence of excess variants of H_6-ϵ. Each data set was fit to the equation, $v = V/(1 + [\text{azide}]/K_I)$, and then ATPase rates were normalized to V (μmol·min^{-1}·mg^{-1} $F_1(-\delta\epsilon)$, without azide) = 100%. Without ϵ, similar K_I values (μM) were obtained for assays done with 2:1 mM ATP/Mg^{2+} ($V = 78 \pm 3$, $K_I = 4.7 \pm 0.7$, not shown) or 1:2 mM ATP/Mg^{2+} (○; *dashed line*, $V = 29.3 \pm 0.5$, $K_I = 5.3 \pm 0.3$). Assays were done with 1:2 mM ATP/Mg^{2+} in the presence of 100 nM wild-type ϵ (●; $V = 3.8 \pm 0.04$, $K_I = 24.5 \pm 0.9$) or 100 nM ϵ88stop (△; $V = 17.9 \pm 0.3$, $K_I = 4.6 \pm 0.2$) or with 2:1 mM ATP/Mg^{2+} in the presence of 100 nM ϵA101C/L121C + 5 mM DTT (▼; $V = 30.9 \pm 0.3$, $K_I = 13.5 \pm 0.4$) or in the presence of 300 nM disulfide-bonded ϵA101C/L121C (▽; $V = 75.6 \pm 0.7$, $K_I = 6.2 \pm 0.2$). In control assays (not shown), 5 mM DTT had no direct effect on ATPase activity of $F_1(-\delta\epsilon)$.

DISCUSSION

Correlating Results with Functional and Rotational States of the Enzyme—Hydrolysis by the three alternating catalytic sites of F_1 drives a full 360° rotation of the γ central rotary shaft, so hydrolysis of each ATP molecule involves a 120° rotation of γ relative to $\alpha_3\beta_3$. As depicted schematically in Fig. 9, SM microscopy studies of bacterial F_1-ATPases (reviewed in Refs. 62 and 63) have shown that each 120° rotation is comprised of two observable rotary substeps (*solid arrows*); MgATP binding at one alternating catalytic site drives an ~80° rotation of γ to the catalytic dwell angle, whereas the subsequent ~40° rotation is limited by the intrinsic rates of hydrolysis and P_i dissociation at the other alternating catalytic sites. At 120°, Mg^{2+} and ADP dissociate from one site before or in concert with binding of MgATP at another site to drive the next 80° substep. Fig. 9 also includes *bars* along the rotational arc that depict the observed angular position of γ (relative to $\alpha_3\beta_3$) in crystal structures of F_1 or F_1·*c*-ring complexes. This is based on alignment of structures by a structurally conserved, apparently stiff core of the γ subunit that we identified previously (8). A recent analysis of MF_1 structures concluded that the position of γ could not be correlated with rotational angle during the catalytic cycle, arguing that the part of γ protruding below $\alpha_3\beta_3$ is variably displaced by lattice contacts in different crystals (64). However, biophysical characterization of the stiffness of γ indicates that only the lowest portion of γ, near its interface with the *c*-ring of F_O, is extremely pliable (65). Also, the 99 residues of γ that we identified as a structurally conserved "γ-core" include (i) most of the γ coiled-coil that is inside $\alpha_3\beta_3$, (ii) the first ~15 residues of the γ C-terminal helix that protrude below $\alpha_3\beta_3$, and (iii) 41 residues of the γ Rossmann fold domain that pack beside the protruding part of the γ C-terminal helix (see supplemental Figs. 4 and 5 of Ref. 8). We have updated our analysis of the rotational angle of γ to include 34 F_1 or F_1·*c*-ring structures and find that all γ subunits superimpose well with the γ-core (supplemental Table S-I). Thus, the distribution of F_1 structures along the rotary arc of γ in Fig. 9 should be useful for comparing structural states with functional and rotational data.

Although there is no current consensus for correlating the rotary position of γ in known structures with the dwell states observed in SM assays after 80 and 40° substeps (63, 66, 67), we

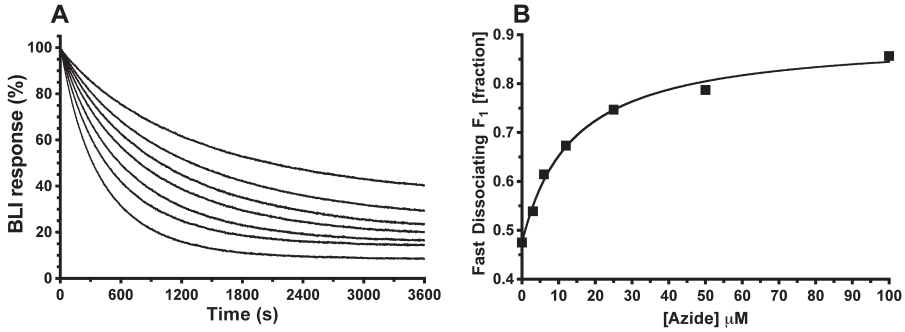

FIGURE 8. **Effects of azide on dissociation of F_1 from sensor-bound, wild-type ϵ.** *A*, kinetics for F_1·ϵ dissociation measured by BLI. Prior to the F_1 dissociation phase shown, BLI sensors had been loaded with biotinylated wild-type ϵ and then incubated for 900 s in buffer with 20 nM $F_1(-\delta\epsilon)$; the normalized BLI signal at time 0 represents bound $F_1(-\delta\epsilon)$. Dissociation of $F_1(-\delta\epsilon)$ from immobilized ϵ was done in hydrolysis conditions (1 mM ATP, 2 mM Mg^{2+}) with increasing concentrations of azide, as indicated. Dissociation kinetics were biphasic, with "fast" ($1–2.5 \times 10^{-3}$ s^{-1}) and "slow" ($0.8–1.6 \times 10^{-4}$ s^{-1}) fractions (nonlinear regression fits not shown but essentially superimpose with data at scale shown; $R^2 > 0.9995$ for all fits). *B*, the azide dependence of F_1·ϵ dissociation. The fraction of complexes that dissociated fast *versus* slow shows hyperbolic dependence on azide concentration, with $K_{½} = 14 \pm 2.3$ μM; $R^2 = 0.9935$.

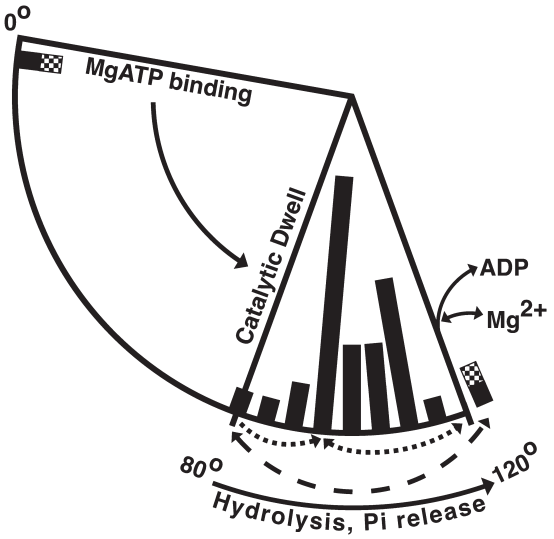

FIGURE 9. **Proposed paths for inhibition by ϵCTD or ADP/azide, relative to rotary catalytic substeps and angular positions of γ in F_1 structures.** A 120° segment is shown for the γ rotational cycle, corresponding to net hydrolysis of 1 ATP. Two rotary substeps, observed by SM microscopy, are depicted by *solid arrows* (direction is for rotation of γ during hydrolysis). *Bars* along the *inner edge* of the 80–120° *arc* indicate the rotary angle of γ in 34 F_1 crystal structures (see supplemental Table S-I). *Bars* are spaced every 5°, and the *height* represents the number of F_1 structures aligned near each angle ± 2.5°; *shortest bar*, one structure; *longest bar*, 12 structures. *Bars* are *shaded* for structures of bovine F_1 (*black*), yeast F_1 (*gray*), and *E. coli* F_1 (*checkered*). The *dotted arrows below* the *bars* indicate the proposed paths to and from the ADP-inhibited state, as stabilized by azide at ~95° (61). The *dashed arrow* shows the ~40° rotary shift proposed to occur during transition into (*counterclockwise*) or out of (*clockwise*) the ϵ-inhibited state. The two F_1 aligned past 120° are also shown near 0° because this position should be the starting point for the next 120° turn.

assign γ to be at 80° for one MF_1 structure, with all three catalytic sites filled with nucleotide (Protein Data Bank entry 1H8E), because structural considerations (68) and molecular dynamics simulations (69) suggest that it is closest to the catalytic dwell state. Most MF_1 structures have no nucleotide in the β_E site due to an open conformation that distorts the nucleotide-binding pocket, but 1H8E has a "half-closed" conformation of β_E with bound MgADP and SO_4^{2-} (thought to mimic P_i binding). Another recent MF_1 structure (Protein Data Bank entry 4ASU) also has a nucleotide in all three catalytic sites, but its β_E is much closer to the open conformation and has ADP but no bound SO_4^{2-} (or P_i) or Mg^{2+} (64). The 4ASU structure was proposed to represent the catalytic intermediate from which final products Mg^{2+} and ADP dissociate, and its rotary position at ~123° (Fig. 9) correlates with SM studies indicating that ADP dissociates after ~40° rotation to one of the 120° dwell positions (70–72). The structural indication that Mg^{2+} dissociates before ADP (64) suggests that the inhibitory effect of free Mg^{2+} occurs at the 120° position. This can explain results showing that excess free Mg^{2+} does not affect inhibitory transitions that occur at the catalytic dwell step at 80°; free Mg^{2+} does not affect the rate at which actively rotating *E. coli* $F_1(-\epsilon)$ switches to the ADP-inhibited (paused) state (22), and, as shown here, free Mg^{2+} does not alter inhibition of *E. coli* F_1 by ϵCTD or azide.

Although our results indicate that ADP and ϵ inhibition begin as competing processes after hydrolysis at the catalytic dwell, F_1 structures of these inhibited states have γ positioned at angles that are distinct from the catalytic dwell; in Fig. 9, azide-inhibited MF_1 (61) has γ at 93°, and ϵ-inhibited *E. coli* F_1 (8) has γ rotated much further to 123° (*checkered bar*). In contrast, SM studies concluded that both ADP and ϵ inhibition cause long paused/inactive states at the catalytic dwell at 80° (22–24, 57). With a bead attached to γ or ϵ, it is possible that SM microscopy could have overlooked dynamic oscillations between 80 and 120° because those assays can exhibit broad angular distributions of events. For example, during long paused periods (up to 1–2 s) without net rotation, a γ-attached bead on *E. coli* $F_1(-\epsilon)$ showed rapid, ongoing angular fluctuations spanning at least ±30° (Fig. 3*A* in Ref. 22). This could represent dynamic rotational oscillations in *E. coli* F_1 or could be a technical limitation because the bead was attached to γ by a single cysteine, allowing for significant flexibility in the linkage. On the other hand, there is prior evidence that functional rotation is needed for transition to and from the ϵ-inhibited state; with *E. coli* F_OF_1 in liposomes, a chemical treatment that blocks rotation of F_O also prevented nucleotide-dependent changes in the conformation of ϵ (54). With F_1 exposed to MgADP/P_i, conditions that stabilize the ϵ-inhibited state (Fig. 5), cryoelectron microscopy of *E. coli* F_1 showed a unique, ϵ-dependent position of γ and a unique position of ϵ relative to $\alpha_3\beta_3$ (73). Also, with F_OF_1-liposomes, SM fluorescence assays showed a shift in the position of the ϵ NTD relative to the F_O stator for active *versus* inactive complexes (74). Thus, we propose that the ϵCTD begins inserting into bacterial F_1 near the catalytic dwell (80°) but then induces partial rotation to ~120° to achieve the final ϵ-inhibited state, with the last half of the ϵCTD buried in the central cavity of F_1 (8). This is similar to a proposal that insertion of the mitochondrial inhibitor protein (IF_1) into MF_1 involves rotational steps (75), and IF_1-inhibited MF_1 has γ rotated ~27° past the catalytic dwell in Fig. 9. The transitions of azide-inhibited MF_1 and ϵ-inhibited *E. coli* F_1 to distinct rotary angles may help explain the competition between these inhibitory paths. Azide-inhibited MF_1 has azide bound with MgADP in the closed, high affinity β_D site, but azide inhibition is unlikely to occur in the ϵ-inhibited state of *E. coli* F_1 because insertion of the ϵCTD and rotation of γ shift β_D to a distinct "half-closed" conformation. Conversely, if *E. coli* F_1 first shifted to the ADP-inhibited state, azide would probably stabilize the closed β_D state and so prevent opening of the $\alpha_E\beta_D$ interface with γ that is necessary to allow insertion of the ϵCTD. In Fig. 9, the *broken lines below* the *arc* indicate the proposed rotational paths leading to and from ADP- or ϵ-inhibited states. In SM tests of forced rotation, TF_1 was preferentially activated from the ADP-inhibited state (paused at ~93°; Fig. 9) by >40° rotation forward, and, consistent with proposed release of ADP near 120° (Fig. 9), added ADP suppressed or reversed rotational activation (76). In contrast, forced rotation of up to 120° in either direction failed to reactivate ϵ-paused TF_1 (26). Based on the asymmetric insertion of ϵCTD within F_1 (8), we suspect that reactivation from the ϵ_X-inhibited state (Fig. 9, near 120°) occurs with the lowest activation barrier by reverse rotation of γ/ϵNTD toward the catalytic dwell angle at 80° (Fig. 9, *dashed arrow*). Such reactivation by rotation in the direction of ATP synthesis may be indicated by a study with *E. coli* F_OF_1-liposomes; with MgADP and P_i present, prior exposure to pro-

ton motive force activated the initial rate of subsequent ATPase activity up to 9-fold (77).

Dynamics of ε Conformational Changes and the Influence of Nucleotides/Ligands—Under conditions for ATP hydrolysis, SM assays with a 60-nm gold bead attached to γ showed that *E. coli* F_1 complexes switch back and forth between actively rotating and paused states every few seconds, with or without ε bound to F_1 (22). Our results on F_1•ε dissociation kinetics are consistent with such rapid exchange between active and inactive states. As shown in Fig. 5 (*C* and *D*), there were no more than a few seconds lag in ligand-dependent switching between the slowest and fastest modes of F_1•ε dissociation. Exposure to saturating nucleotide without hydrolysis (ATP/EDTA or MgAMPPNP) induced the fastest and essentially monophasic F_1•ε dissociation (Figs. 5 and 6), indicating that few F_1•ε complexes remained in or could regain access to the ε_X-inhibited state. However, most F_1•ε complexes still dissociated slowly upon exposure to hydrolysis conditions (Fig. 5), consistent with noncompetitive inhibition by ε *versus* ATP for *E. coli* F_1 (29, 44). Also, the K_I for ε inhibition of steady-state hydrolysis (Table 1, ~0.5 nM) is similar to the K_D for F_1•ε binding (Table 2, 0.24 nM), which was measured without added nucleotides. Thus, it is unlikely that catalytic binding of ATP or MgAMPPNP directly increases the rate at which the ε_X-paused state returns to an active form. Rather, we propose that the intrinsic rates to and from the ε_X-inhibited state are fast enough (seconds or less) to allow ligands to influence subsequent conformational changes once F_1 exits from the ε-inhibited state. Once the εCTD escapes from the central cavity of F_1 near 80°, F_1 would be most likely to rotate forward, completing an active 40° step (Fig. 9, *solid arrow*). At that point, binding of nucleotide would drive an ~80° step toward the next catalytic dwell but, without hydrolysis, would trap F_1 in a conformation and rotary position that would not allow the εCTD to reinsert; thus, F_1•ε complexes would dissociate at the faster rate observed with only γ/εNTD interactions. With hydrolysis conditions, each return to a catalytic dwell step would provide the same low probability for insertion of the εCTD, and, as indicated by SM studies (22), the long durations of the paused/inhibited states (1 to 3.5 s) relative to the limiting catalytic steps (1–2 ms) would result in a large fraction of inhibited complexes during steady-state hydrolysis.

In an SM study with *E. coli* F_1 (22), the presence of ε did not alter the duration time of active complexes (0.5–1 s), but ε-paused states had longer duration times (up to 3.5 s) than ADP-paused states (~1 s). This is consistent with other indications that ε inhibition predominates over ADP inhibition. Oxyanions, which are thought to activate F_1 by promoting release of inhibitory ADP (78), activate *E. coli* F_1 more if ε is absent (28), and recently it was shown that the oxyanion selenite optimally activates ε-depleted *E. coli* F_1 ~10-fold[4] with excess free Mg^{2+} present but only activates ε-saturated F_1 2–2.5-fold (79). Also, because our results show that inhibition by the εCTD is distinct from the ADP-inhibited transition, the unaffected duration of the active state (22) suggests that a prior common step is rate-limiting for transitions to either ADP- or ε-inhibited states. This common step is probably the end of hydrolysis that precedes P_i release because ε reduces the rate of P_i release ~15-fold following "unisite" hydrolysis (28). P_i stabilizes F_1 with ε in the ε_X state, which could mean that P_i rebinds to β_D (with bound MgADP) and delays an active 40° rotation, allowing more time for a possible transition to the ε_X-inhibited state. However, we cannot rule out that the P_i effect could be due in part to binding to other β(s), which show SO_4^{3-} bound at the "P-loop" in ε-inhibited F_1 (8).

Conclusions—This study sheds further light on how the CTD of subunit ε inhibits the catalytic F_1 complex of a bacterial ATP synthase. Most significantly, results reveal that ATP hydrolysis is required for insertion of the inhibitory εCTD into F_1 at the catalytic dwell step and that ε inhibition competes with conversion to an ADP-inhibited state of the enzyme. With insertion of the εCTD starting at the catalytic dwell (~80°), the dynamic response of the conformation of ε to catalytic site ligands and the structurally observed γ angle of ~123° in ε-inhibited F_1 suggest dynamic, reversible rotation over the 40° substep. Our results also show that the εCTD has a small energetic contribution to net binding of ε to F_1. Thus, there is potential for antibiotic development by discovering or designing compounds that enhance or mimic ε inhibition of bacterial ATP synthases. The BLI assays established here for kinetics of F_1•ε binding and dissociation should be valuable in further analyzing which εCTD residues and interactions are critical for ε inhibition in F_1-ATPase from *E. coli* and other bacteria. Of course, the BLI assay cannot be used to study ε inhibition in membrane-bound ATP synthase because ε does not dissociate from intact F_OF_1. The extent of ε inhibition can vary widely for membranes isolated from different bacteria. For example, *E. coli* membranes exhibit substantial ATPase activity, whereas mycobacterial membranes are devoid of ATPase activity but can be activated by treatment that probably damages the ε subunit (80). Thus, additional approaches will be needed to determine what other factors influence ε inhibition in ATP synthases of different bacterial species.

Acknowledgments—We thank Y. M. Milgrom for stimulating discussions and for sharing unpublished results. We thank Profs. Richard L. Cross and Stephan Wilkens for critical reading of the manuscript. We thank Prof. Robert K. Nakamoto (University of Virginia) for plasmid $pH_6\varepsilon$.

[4] Y. M. Milgrom, personal communication.

REFERENCES

1. Boyer, P. D. (1997) The ATP synthase. A splendid molecular machine. *Annu. Rev. Biochem.* **66,** 717–749
2. Duncan, T. M. (2004) The ATP Synthase. Parts and Properties of a Rotary Motor. in *The Enzymes*, Vol. XXIII, 3rd Ed. (Hackney, D. D., and Tamanoi, F., eds) pp. 203–275, Elsevier Academic Press, New York
3. Spetzler, D., Ishmukhametov, R., Hornung, T., Martin, J., York, J., Jin-Day, L., and Frasch, W. D. (2012) *Energy Transduction by the Two Molecular Motors of the F_OF_1 ATP Synthase* (Eaton-Rye, J. J., Tripathy, B. C., and Sharkey, T. D., eds) pp. 561–590, Springer, Dordrecht, Netherlands
4. Cox, G. B., Devenish, R. J., Gibson, F., Howitt, S. M., and Nagley, P. (1992) The structure and assembly of ATP synthase. in *Molecular Mechanisms in Bioenergetics* (Ernster, L., ed) pp. 283–315, Elsevier Science, New York
5. Andries, K., Verhasselt, P., Guillemont, J., Göhlmann, H. W., Neefs, J. M., Winkler, H., Van Gestel, J., Timmerman, P., Zhu, M., Lee, E., Williams, P.,

de Chaffoy, D., Huitric, E., Hoffner, S., Cambau, E., Truffot-Pernot, C., Lounis, N., and Jarlier, V. (2005) A diarylquinoline drug active on the ATP synthase of *Mycobacterium tuberculosis*. *Science* **307,** 223–227
6. Koul, A., Vranckx, L., Dendouga, N., Balemans, W., Van den Wyngaert, I., Vergauwen, K., Göhlmann, H. W., Willebrords, R., Poncelet, A., Guillemont, J., Bald, D., and Andries, K. (2008) Diarylquinolines are bactericidal for dormant mycobacteria as a result of disturbed ATP homeostasis. *J. Biol. Chem.* **283,** 25273–25280
7. Diacon, A. H., Pym, A., Grobusch, M., Patientia, R., Rustomjee, R., Page-Shipp, L., Pistorius, C., Krause, R., Bogoshi, M., Churchyard, G., Venter, A., Allen, J., Palomino, J. C., De Marez, T., van Heeswijk, R. P., Lounis, N., Meyvisch, P., Verbeeck, J., Parys, W., de Beule, K., Andries, K., and Mc Neeley, D. F. (2009) The diarylquinoline TMC207 for multidrug-resistant tuberculosis. *N. Engl. J. Med.* **360,** 2397–2405
8. Cingolani, G., and Duncan, T. M. (2011) Structure of the ATP synthase catalytic complex (F_1) from *Escherichia coli* in an autoinhibited conformation. *Nat. Struct. Mol. Biol.* **18,** 701–707
9. Feniouk, B. A., Suzuki, T., and Yoshida, M. (2006) The role of subunit ε in the catalysis and regulation of F_OF_1-ATP synthase. *Biochim. Biophys. Acta* **1757,** 326–338
10. Richter, M. L. (2004) γ-ε interactions regulate the chloroplast ATP synthase. *Photosynth. Res.* **79,** 319–329
11. Campanella, M., Casswell, E., Chong, S., Farah, Z., Wieckowski, M. R., Abramov, A. Y., Tinker, A., and Duchen, M. R. (2008) Regulation of mitochondrial structure and function by the F_1F_O-ATPase inhibitor protein, IF_1. *Cell Metab.* **8,** 13–25
12. Iino, R., Hasegawa, R., Tabata, K. V., and Noji, H. (2009) Mechanism of inhibition by C-terminal α-helices of the ε subunit of *Escherichia coli* F_OF_1-ATP synthase. *J. Biol. Chem.* **284,** 17457–17464
13. Masaike, T., Suzuki, T., Tsunoda, S. P., Konno, H., and Yoshida, M. (2006) Probing conformations of the β subunit of F_OF_1-ATP synthase in catalysis. *Biochem. Biophys. Res. Commun.* **342,** 800–807
14. Stocker, A., Keis, S., Vonck, J., Cook, G. M., and Dimroth, P. (2007) The Structural basis for unidirectional rotation of thermoalkaliphilic F_1-ATPase. *Structure* **15,** 904–914
15. Gibbons, C., Montgomery, M. G., Leslie, A. G., and Walker, J. E. (2000) The structure of the central stalk in bovine F_1-ATPase at 2.4 Å resolution. *Nat. Struct. Biol.* **7,** 1055–1061
16. Kabaleeswaran, V., Puri, N., Walker, J. E., Leslie, A. G., and Mueller, D. M. (2006) Novel features of the rotary catalytic mechanism revealed in the structure of yeast F_1 ATPase. *EMBO J.* **25,** 5433–5442
17. Uhlin, U., Cox, G. B., and Guss, J. M. (1997) Crystal structure of the ε subunit of the proton-translocating ATP synthase from *Escherichia coli*. *Structure* **5,** 1219–1230
18. Wilkens, S., and Capaldi, R. A. (1998) Solution structure of the ε subunit of the F_1-ATPase from *Escherichia coli* and interactions of this subunit with β subunits in the complex. *J. Biol. Chem.* **273,** 26645–26651
19. Yagi, H., Kajiwara, N., Tanaka, H., Tsukihara, T., Kato-Yamada, Y., Yoshida, M., and Akutsu, H. (2007) Structures of the thermophilic F_1-ATPase ε subunit suggesting ATP-regulated arm motion of its C-terminal domain in F_1. *Proc. Natl. Acad. Sci. U.S.A.* **104,** 11233–11238
20. Watt, I. N., Montgomery, M. G., Runswick, M. J., Leslie, A. G., and Walker, J. E. (2010) Bioenergetic cost of making an adenosine triphosphate molecule in animal mitochondria. *Proc. Natl. Acad. Sci. U.S.A.* **107,** 16823–16827
21. Schulenberg, B., and Capaldi, R. A. (1999) The ε subunit of the F_1F_O complex of *Escherichia coli*. Cross-linking studies show the same structure *in situ* as when isolated. *J. Biol. Chem.* **274,** 28351–28355
22. Sekiya, M., Hosokawa, H., Nakanishi-Matsui, M., Al-Shawi, M. K., Nakamoto, R. K., and Futai, M. (2010) Single molecule behavior of inhibited and active states of *Escherichia coli* ATP synthase F_1 rotation. *J. Biol. Chem.* **285,** 42058–42067
23. Konno, H., Murakami-Fuse, T., Fujii, F., Koyama, F., Ueoka-Nakanishi, H., Pack, C. G., Kinjo, M., and Hisabori, T. (2006) The regulator of the F_1 motor. Inhibition of rotation of cyanobacterial F_1-ATPase by the ε subunit. *EMBO J.* **25,** 4596–4604
24. Tsumuraya, M., Furuike, S., Adachi, K., Kinosita, K., Jr., and Yoshida, M. (2009) Effect of ε subunit on the rotation of thermophilic *Bacillus* F_1-ATPase. *FEBS Lett.* **583,** 1121–1126
25. Konno, H., Isu, A., Kim, Y., Murakami-Fuse, T., Sugano, Y., and Hisabori, T. (2011) Characterization of the relationship between ADP- and ε-induced inhibition in cyanobacterial F_1-ATPase. *J. Biol. Chem.* **286,** 13423–13429
26. Saita, E. I., Iino, R., Suzuki, T., Feniouk, B. A., Kinosita, K., Jr., and Yoshida, M. (2010) Activation and stiffness of the inhibited states of F_1-ATPase probed by single-molecule manipulation. *J. Biol. Chem.* **285,** 11411–11417
27. Feniouk, B. A., Suzuki, T., and Yoshida, M. (2007) Regulatory interplay between proton motive force, ADP, phosphate, and subunit ε in bacterial ATP synthase. *J. Biol. Chem.* **282,** 764–772
28. Dunn, S. D., Zadorozny, V. D., Tozer, R. G., and Orr, L. E. (1987) ε subunit of *Escherichia coli* F_1-ATPase. Effects on affinity for aurovertin and inhibition of product release in unisite ATP hydrolysis. *Biochemistry* **26,** 4488–4493
29. Weber, J., Dunn, S. D., and Senior, A. E. (1999) Effect of the ε-subunit on nucleotide binding to *Escherichia coli* F_1-ATPase catalytic sites. *J. Biol. Chem.* **274,** 19124–19128
30. Andrews, S. H., Peskova, Y. B., Polar, M. K., Herlihy, V. B., and Nakamoto, R. K. (2001) Conformation of the γ subunit at the γ-ε-c interface in the complete *Escherichia coli* F_1-ATPase complex by site-directed spin labeling. *Biochemistry* **40,** 10664–10770
31. Cipriano, D. J., and Dunn, S. D. (2006) The role of the ε subunit in the *Escherichia coli* ATP synthase. The C-terminal domain is required for efficient energy coupling. *J. Biol. Chem.* **281,** 501–507
32. Tsao, K.-L., DeBarbieri, B., Michel, H., and Waugh, D. S. (1996) A versatile plasmid expression vector for the production of biotinylated proteins by site-specific, enzymatic modification in *Escherichia coli*. *Gene* **169,** 59–64
33. Bhardwaj, A., Walker-Kopp, N., Wilkens, S., and Cingolani, G. (2008) Foldon-guided self-assembly of ultra-stable protein fibers. *Protein Sci.* **17,** 1475–1485
34. Duncan, T. M., Zhou, Y., Bulygin, V. V., Hutcheon, M. L., and Cross, R. L. (1995) Probing interactions of the *Escherichia coli* F_OF_1 ATP synthase β and γ subunits with disulphide cross-links. *Biochem. Soc. Trans.* **23,** 736–741
35. Laemmli, U. K. (1970) Cleavage of structural proteins during the assembly of the head of bacteriophage T4. *Nature* **227,** 680–685
36. Peterson, G. L. (1977) A simplification of the protein assay method of Lowry *et al.* which is more generally applicable. *Anal. Biochem.* **83,** 346–356
37. Dunn, S. D. (1986) Removal of the ε subunit from *Escherichia coli* F_1-ATPase using monoclonal anti-ε antibody affinity chromatography. *Anal. Biochem.* **159,** 35–42
38. Duncan, T. M., Bulygin, V. V., Zhou, Y., Hutcheon, M. L., and Cross, R. L. (1995) Rotation of subunits during catalysis by *Escherichia coli* F_1-ATPase. *Proc. Natl. Acad. Sci. U.S.A.* **92,** 10964–10968
39. Penefsky, H. S. (1977) Reversible binding of P_i by beef heart mitochondrial adenosine triphosphatase. *J. Biol. Chem.* **252,** 2891–2899
40. Pullman, M. E., Penefsky, H. S., Datta, A., and Racker, E. (1960) Partial resolution of the enzymes catalysing oxidative phosphorylation. I. Purification and properties of soluble dinitrophenyl-stimulated adonosine triphophatase. *J. Biol. Chem.* **235,** 3322–3329
41. Abdiche, Y., Malashock, D., Pinkerton, A., and Pons, J. (2008) Determining kinetics and affinities of protein interactions using a parallel real-time label-free biosensor, the Octet. *Anal. Biochem.* **377,** 209–217
42. Tozer, R. G., and Dunn, S. D. (1986) Column centrifugation generates an intersubunit disulfide bridge in *Escherichia coli* F_1-ATPase. *Eur. J. Biochem.* **161,** 513–518
43. Dunn, S. D. (1982) The isolated γ subunit of *Escherichia coli* F_1 ATPase binds the ε subunit. *J. Biol. Chem.* **257,** 7354–7359
44. Sternweis, P. C., and Smith, J. B. (1980) Characterization of the inhibitory ε subunit of the proton-translocating adenosine triphosphatase from *Escherichia coli*. *Biochemistry* **19,** 526–531
45. Hyndman, D. J., Milgrom, Y. M., Bramhall, E. A., and Cross, R. L. (1994) Nucleotide-binding sites on *Escherichia coli* F_1-ATPase. Specificity of noncatalytic sites and inhibition at catalytic sites by MgADP. *J. Biol. Chem.* **269,** 28871–28877
46. Kato, Y., Sasayama, T., Muneyuki, E., and Yoshida, M. (1995) Analysis of

time-dependent change of *Escherichia coli* F_1-ATPase activity and its relationship with apparent negative cooperativity. *Biochim. Biophys. Acta* **1231,** 275–281
47. Jault, J. M., Matsui, T., Jault, F. M., Kaibara, C., Muneyuki, E., Yoshida, M., Kagawa, Y., and Allison, W. S. (1995) The $\alpha_3\beta_3\gamma$ complex of the F_1-ATPase from thermophilic *Bacillus PS3* containing the α D261N substitution fails to dissociate inhibitory MgADP from a catalytic site when ATP binds to noncatalytic sites. *Biochemistry* **34,** 16412–16418
48. Drobinskaya, I. Y., Kozlov, I. A., Murataliev, M. B., and Vulfson, E. N. (1985) Tightly bound adenosine diphosphate, which inhibits the activity of mitochondrial F_1-ATPase, is located at the catalytic site of the enzyme. *FEBS Lett.* **182,** 419–424
49. Milgrom, Y. M., and Boyer, P. D. (1990) The ADP that binds tightly to nucleotide-depleted mitochondrial F_1-ATPase and inhibits catalysis is bound at a catalytic site. *Biochim. Biophys. Acta* **1020,** 43–48
50. Murataliev, M. B., Milgrom, Y. M., and Boyer, P. D. (1991) Characteristics of the combination of inhibitory Mg^{2+} and azide with the F_1 ATPase from chloroplasts. *Biochemistry* **30,** 8305–8310
51. Guerrero, K. J., Xue, Z. X., and Boyer, P. D. (1990) Active/Inactive state transitions of the chloroplast F_1 ATPase are induced by a slow binding and release of Mg^{2+}. Relationship to catalysis and control of F_1 ATPases. *J. Biol. Chem.* **265,** 16280–16287
52. Jault, J. M., Divita, G., Allison, W. S., and Di Pietro, A. (1993) Glutamine 170 to tyrosine substitution in yeast mitochondrial F_1 β-subunit increases catalytic site interaction with GDP and IDP and produces negative cooperativity of GTP and ITP hydrolysis. *J. Biol. Chem.* **268,** 20762–20767
53. Xiong, H., Zhang, D., and Vik, S. B. (1998) Subunit ϵ of the *Escherichia coli* ATP synthase. Novel insights into structure and function by analysis of thirteen mutant forms. *Biochemistry* **37,** 16423–16429
54. Mendel-Hartvig, J., and Capaldi, R. A. (1991) Nucleotide-dependent and dicyclohexylcarbodiimide-sensitive conformational changes in the ϵ subunit of *Escherichia coli* ATP synthase. *Biochemistry* **30,** 10987–10991
55. Mendel-Hartvig, J., and Capaldi, R. A. (1991) Catalytic site nucleotide and inorganic phosphate dependence of the conformation of the ϵ subunit in *Escherichia coli* adenosinetriphosphatase. *Biochemistry* **30,** 1278–1284
56. Dallmann, H. G., Flynn, T. G., and Dunn, S. D. (1992) Determination of the 1-ethyl-3-[(3-dimethylamino)propyl]-carbodiimide-induced cross-link between the β and ϵ subunits of *Escherichia coli* F_1-ATPase. *J. Biol. Chem.* **267,** 18953–18960
57. Hirono-Hara, Y., Noji, H., Nishiura, M., Muneyuki, E., Hara, K. Y., Yasuda, R., Kinosita, K., Jr., and Yoshida, M. (2001) Pause and rotation of F_1-ATPase during catalysis. *Proc. Natl. Acad. Sci. U.S.A.* **98,** 13649–13654
58. Nakanishi-Matsui, M., Kashiwagi, S., Ubukata, T., Iwamoto-Kihara, A., Wada, Y., and Futai, M. (2007) Rotational catalysis of *Escherichia coli* ATP synthase F_1 sector. Stochastic fluctuation and a key domain of the β subunit. *J. Biol. Chem.* **282,** 20698–20704
59. Vasilyeva, E. A., Minkov, I. B., Fitin, A. F., and Vinogradov, A. D. (1982) Kinetic mechanism of mitochondrial adenosine triphosphatase. Inhibition by azide and activation by sulphite. *Biochem. J.* **202,** 15–23
60. Murataliev, M. B., and Boyer, P. D. (1992) The mechanism of stimulation of MgATPase activity of chloroplast F_1-ATPase by non-catalytic adenine-nucleotide binding. Acceleration of the ATP-dependent release of inhibitory ADP from a catalytic site. *Eur. J. Biochem.* **209,** 681–687
61. Bowler, M. W., Montgomery, M. G., Leslie, A. G., and Walker, J. E. (2006) How azide inhibits ATP hydrolysis by the F-ATPases. *Proc. Natl. Acad. Sci. U.S.A.* **103,** 8646–8649
62. Noji, H., Okuno, D., and Ikeda, T. (2011) Mechanochemistry of F_1 motor protein. *Chem. Sci.* **2,** 2086–2093
63. Kinosita, K., Jr. (2012) F_1-ATPase. A prototypical rotary molecular motor. *Adv. Exp. Med. Biol.* **726,** 5–16
64. Rees, D. M., Montgomery, M. G., Leslie, A. G., and Walker, J. E. (2012) Structural evidence of a new catalytic intermediate in the pathway of ATP hydrolysis by F_1-ATPase from bovine heart mitochondria. *Proc. Natl. Acad. Sci. U.S.A.* **109,** 11139–11143
65. Sielaff, H., Rennekamp, H., Wächter, A., Xie, H., Hilbers, F., Feldbauer, K., Dunn, S. D., Engelbrecht, S., and Junge, W. (2008) Domain compliance and elastic power transmission in rotary F_OF_1-ATPase. *Proc. Natl. Acad. Sci. U.S.A.* **105,** 17760–17765
66. Okuno, D., Fujisawa, R., Iino, R., Hirono-Hara, Y., Imamura, H., and Noji, H. (2008) Correlation between the conformational states of F_1-ATPase as determined from its crystal structure and single-molecule rotation. *Proc. Natl. Acad. Sci. U.S.A.* **105,** 20722–20727
67. Sielaff, H., Rennekamp, H., Engelbrecht, S., and Junge, W. (2008) Functional halt positions of rotary F_OF_1-ATPase correlated with crystal structures. *Biophys. J.* **95,** 4979–4987
68. Menz, R. I., Walker, J. E., and Leslie, A. G. (2001) Structure of bovine mitochondrial F_1-ATPase with nucleotide bound to all three catalytic sites. Implications for the mechanism of rotary catalysis. *Cell* **106,** 331–341
69. Pu, J., and Karplus, M. (2008) How subunit coupling produces the γ-subunit rotary motion in F_1-ATPase. *Proc. Natl. Acad. Sci. U.S.A.* **105,** 1192–1197
70. Nishizaka, T., Oiwa, K., Noji, H., Kimura, S., Muneyuki, E., Yoshida, M., and Kinosita, K., Jr. (2004) Chemomechanical coupling in F_1-ATPase revealed by simultaneous observation of nucleotide kinetics and rotation. *Nat. Struct. Mol. Biol.* **11,** 142–148
71. Adachi, K., Oiwa, K., Nishizaka, T., Furuike, S., Noji, H., Itoh, H., Yoshida, M., and Kinosita, K., Jr. (2007) Coupling of rotation and catalysis in F_1-ATPase revealed by single-molecule imaging and manipulation. *Cell* **130,** 309–321
72. Shimo-Kon, R., Muneyuki, E., Sakai, H., Adachi, K., Yoshida, M., and Kinosita, K., Jr. (2010) Chemo-mechanical coupling in F_1-ATPase revealed by catalytic site occupancy during catalysis. *Biophys. J.* **98,** 1227–1236
73. Wilkens, S., and Capaldi, R. A. (1994) Asymmetry and structural changes in ECF_1 examined by cryoelectronmicroscopy. *Biol. Chem. Hoppe-Seyler* **375,** 43–51
74. Zimmermann, B., Diez, M., Zarrabi, N., Gräber, P., and Börsch, M. (2005) Movements of the ϵ-subunit during catalysis and activation in single membrane-bound H^+-ATP synthase. *EMBO J.* **24,** 2053–2063
75. Gledhill, J. R., Montgomery, M. G., Leslie, A. G., and Walker, J. E. (2007) How the regulatory protein, IF_1, inhibits F_1-ATPase from bovine mitochondria. *Proc. Natl. Acad. Sci. U.S.A.* **104,** 15671–15676
76. Hirono-Hara, Y., Ishizuka, K., Kinosita, K., Jr., Yoshida, M., and Noji, H. (2005) Activation of pausing F_1 motor by external force. *Proc. Natl. Acad. Sci. U.S.A.* **102,** 4288–4293
77. Fischer, S., Graber, P., and Turina, P. (2000) The activity of the ATP synthase from *Escherichia coli* is regulated by the transmembrane proton motive force. *J. Biol. Chem.* **275,** 30157–30162
78. Milgrom, Y. M., and Cross, R. L. (1993) Nucleotide binding sites on beef heart mitochondrial F_1-ATPase. Cooperative interactions between sites and specificity of noncatalytic sites. *J. Biol. Chem.* **268,** 23179–23185
79. Bulygin, V. V., and Milgrom, Y. M. (2009) A bi-site mechanism for *Escherichia coli* F_1-ATPase accounts for the observed positive catalytic cooperativity. *Biochim. Biophys. Acta* **1787,** 1016–1023
80. Haagsma, A. C., Driessen, N. N., Hahn, M. M., Lill, H., and Bald, D. (2010) ATP synthase in slow- and fast-growing mycobacteria is active in ATP synthesis and blocked in ATP hydrolysis direction. *FEMS Microbiol. Lett.* **313,** 68–74
81. Pettersen, E. F., Goddard, T. D., Huang, C. C., Couch, G. S., Greenblatt, D. M., Meng, E. C., and Ferrin, T. E. (2004) UCSF Chimera. A visualization system for exploratory research and analysis. *J. Comput. Chem.* **25,** 1605–1612